Acta Acustica 2024, **8**, 23
© The Author(s), Published by EDP Sciences, 2024
https://doi.org/10.1051/aacus/2024016

Available online at:
https://acta-acustica.edpsciences.org

SCIENTIFIC ARTICLE OPEN ACCESS

Elliptic tangent imaging method for layered plate interfacial defects based on non-dispersive guided waves

Jiaqi Wang, Bing Li*, and Yunfei Zhang

National Key Lab. of Aerospace Power System and Plasma Technology, Xi'an Jiaotong University, No.28, West Xianning Road, Xi'an, Shaanxi 710049, China

Received 23 December 2023, Accepted 12 May 2024

Abstract – Layered structures play an increasingly pivotal role in diverse fields such as aerospace, pipeline transportation, and petrochemical engineering. However, defects situated at the interfaces between layers pose a challenge for conventional Non-Destructive testing (NDT) methods, impeding accurate imaging. This research introduces the elliptic tangent imaging method based on interface wave modes to visualize interfacial defects within layered structures. The interface wave mode, characterized by high-frequency non-dispersive traits, facilitates precise localization of defects. Its energy concentration in the interface enhances sensitivity to interfacial defects. The elliptic tangent imaging method proposed in this paper capitalizes on the transmission coefficients of the oblique incidence technique for surface waves, enabling the concurrent determination of defect location and orientation using one pair of transducers. The application of the orthogonal matched pursuit algorithm for sparse representation of the raw signal further enhances positioning accuracy. This paper establishes an automatic detection system for interface waves, demonstrating swift transducer switching. Experimental validation of wave velocity aligns closely with theoretical calculations. In experiments focusing on interfacial defect imaging in bilayer aluminum-steel plates, the system exhibits the capability to accurately depict interfacial defects with varying orientations.

Keywords: Non-dispersive, Guided waves, Interfacial defects, Defect imaging, Interface wave

1 Introduction

Layered structures are becoming increasingly essential in various fields, including aerospace, pipeline transportation, renewable energy, and petrochemical engineering. Metal multilayers, such as aluminum-steel combinations, offer a blend of different metal properties, combining the strength of steel with the corrosion resistance of aluminum. In critical structures, even minor defects between layers are intolerable. Unfortunately, many commonly used Non-Destructive testing (NDT) methods struggle with evaluating these subtle interfacial defects. Evaluating interfacial defects poses a greater challenge due to the subtle differences in physical characteristics between the interface and the defects. For instance, the intact interface serves as the boundary between two metals, while defects mark the boundaries between metal and air.

Ultrasonic guided waves, with their advantages over other NDT techniques, have garnered significant scholarly interest [1–3]. Based on different phase velocity curves on the dispersion diagram, ultrasonic guided waves roughly divide into Lamb waves [4], surface waves [5], interface waves [6], and other modes [7, 8]. Scholars have explored various guided wave methods to address the NDT challenges posed by layered structures [9–11]. While some focused on simulation or defect identification and localization [12–14], reliable imaging methods for interfacial defects have been scarce.

In the realm of guided wave techniques, the term "non-dispersive" denotes a wave characteristic where different frequency components travel at the same speed. This uniform velocity behavior ensures that different frequencies of the guided wave reach the detection point simultaneously. This coherence simplifies signal interpretation, aiding in the identification and localization of defects, especially in structures with complex geometries or multiple layers [1]. Non-dispersiveness is often linked to specific wave modes, notably surface waves [5] and interface waves [6], in the high-frequency range for multilayer materials. Interface waves concentrate their energy on the interfaces between different media, making them ideal for interfacial defect detection. Meanwhile, there can only be one interface wave mode on each interface. Theoretically, maximizing the excitation frequency of surface and interface waves enables the detection of minor defects on interfaces without concerns about interactions with other wave modes [15, 16].

---

*Corresponding author: `bli@mail.xjtu.edu.cn`

These theoretical insights motivated the exploration of an interface damage imaging method based on interface wave modes to address the intricate challenges posed by interfacial defects mentioned above.

In summary, interface waves possess dual advantages: they are non-dispersive, and their energy is concentrated at the interfaces. In the presence of interfacial defects in a layered structure, multiple conversions occur between surface waves and interface waves during guided wave propagation, leading to reflections and phase variations. However, when the structure is defect-free, received signals should remain nearly identical regardless of the wave pack's travel distance. This stability arises from the non-dispersive nature of interface waves at high frequencies, significantly enhancing the accuracy of abnormal feature extraction and defect reconstruction algorithms.

While imaging interfacial damage in multilayer materials poses greater challenges, there exist several pertinent imaging methods within the domain of ultrasonic guided wave imaging that merit consideration. Examples include the elliptical localization method [17], hyperbolic imaging method [18], concentric circle localization method [19], and others [20]. New imaging methods have also emerged in recent years. The tomographic scanning algorithm stands as a conventional probabilistic imaging technique. This approach employs ultrasonic guided waves to scan a particular layer of a layered structure from various angles. The primary calculation involves assessing the attenuation degree of the guided waves to evaluate the distribution of structural damage within the scanned area [21–23]. On the other hand, the delay-and-sum method is commonly employed for imaging purposes, with a specific focus on utilizing reflected waves [24, 25]. In this context, the defect image is obtained by leveraging crucial information, including wave velocity, the spatial coordinates of the excitation-reception transducer pair, and the echo time when the ultrasonic wave interacts with the defect boundary. While these established imaging methods are valuable references, designing new imaging methods becomes imperative for interface wave modes. These methods must be tailored to accommodate the unique transducer characteristics and damage features associated with interface waves.

The elliptic tangent imaging method presented in this paper leverages the transmission coefficient of the oblique incidence technique for surface waves. The transmission coefficients reflect the effective detection range of the surface transducers. This method enables the simultaneous determination of defect location and orientation using a single pair of transducers. Additionally, the utilization of the orthogonal matched pursuit algorithm for signal sparse representation contributes to improved positioning accuracy. The imaging system demonstrated in this study is proficient in generating single-mode interface waves and accurately identifying interfacial defects of various orientations.

This paper systematically explores the theory and methodology for imaging interfacial defects in layered metal structures based on interface waves, addressing three key aspects: guided wave theory, imaging algorithms, and experimental validations. Section 2 provides concise introductions to guided wave theories in layered plates, accompanied by wave velocity validation experiments for both surface and interface waves. These experiments aim to confirm the guided wave modes generated during the experimental setup. In Section 3, the paper introduces the elliptic tangent imaging method, incorporating the designed approach based on interface waves and the orthogonal matched pursuit algorithm. Section 4 outlines the automatic detection system for interface waves and describes the conducted interfacial defect imaging experiment on a bilayer Al-steel plate. Finally, Section 5 summarizes the main conclusions drawn from the study.

2 Theory and verification of guided waves in multi-layer plates

This section provides a concise overview of the computational methodologies employed to solve dispersion curves and characterize wave structures of ultrasonic guided waves in layered plates, utilizing the global matrix method. The analysis focuses on the distinctive features of surface and interface wave modes within bilayer aluminum-steel plates, incorporating both dispersion theory and experimental verification of wave velocities.

2.1 Global matrix method of guided waves

The displacement vector $\boldsymbol{u}^{(n)}$ within an elastic isotropic homogeneous solid undergoes Helmholtz decomposition, as expressed by equation (1):

$$\begin{cases} \boldsymbol{u}^{(n)} = \nabla\phi_n + \nabla\times\boldsymbol{\Psi}_n \\ \nabla\cdot\boldsymbol{\Psi}_n = 0 \end{cases} \tag{1}$$

Here, $\boldsymbol{u}^{(n)}$ is the displacement vector. n is the number of layers. ϕ_n and $\boldsymbol{\Psi}_n$ are the scalar and vector potentials, respectively. For 2-dimensional problems, displacement vector is reduced to $\boldsymbol{u}^{(n)} = (u_x^{(n)}, u_z^{(n)})$, and $\phi_n = \phi_n(x,z)$. Meanwhile, $\psi_{n,x} = \psi_{n,z} \equiv 0,\ \psi_{n,y} = \psi_{n,y}(x,z)$. Therefore, $\boldsymbol{\Psi}_n$ is hereafter denoted by ψ_n for simplicity.

Considering a stratified structure comprising N layers, depicted in Figure 1 along with relevant geometric parameters, the displacement $u_i^{(n)}$ and stress $\tau_{ij}^{(n)}$ in each layer can be expressed in terms of potentials, as delineated in equation (2):

$$\begin{cases} u_x^{(n)} = \dfrac{\partial\phi_n}{\partial x} + \dfrac{\partial\psi_n}{\partial z} \\ u_z^{(n)} = \dfrac{\partial\phi_n}{\partial z} - \dfrac{\partial\psi_n}{\partial x} \\ \tau_{xx}^{(n)} = \lambda_n(\dfrac{\partial u_x^{(n)}}{\partial x} + \dfrac{\partial u_z^{(n)}}{\partial z}) + 2\mu_n\dfrac{\partial u_x^{(n)}}{\partial x} \\ \tau_{zz}^{(n)} = \lambda_n(\dfrac{\partial u_x^{(n)}}{\partial x} + \dfrac{\partial u_z^{(n)}}{\partial z}) + 2\mu_n\dfrac{\partial u_z^{(n)}}{\partial z} \\ \tau_{xz}^{(n)} = \mu_n(\dfrac{\partial u_z^{(n)}}{\partial x} + \dfrac{\partial u_x^{(n)}}{\partial z}) \end{cases} \tag{2}$$

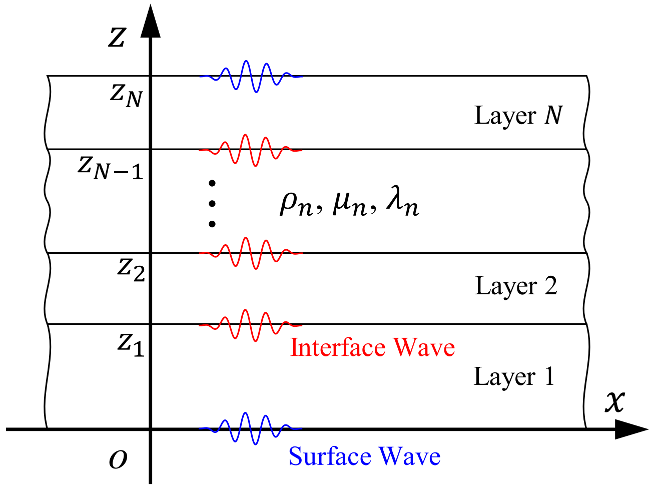

Figure 1. Computational modeling of ultrasonic guided waves in an N-layer plate involves consideration of two surface wave modes on each surface and an interface wave mode at every interface.

Here, λ and μ are the Lame constants, defined by Young's modulus E and Poisson's ratio v as follow:

$$\lambda = \frac{\mu E}{(1+v)(1-2v)}, \ \mu = \frac{E}{2(1+v)}$$

Assuming plane harmonic wave solutions in each layer, as specified in equation (3):

$$\begin{cases} \phi_n = (A_1^{(n)} \mathrm{e}^{-k\alpha_n(z-z_{n-1})} + A_2^{(n)} \mathrm{e}^{k\alpha_n(z-z_n)})\mathrm{e}^{i(kx-\omega t)} \\ \psi_n = (A_3^{(n)} \mathrm{e}^{-k\beta_n(z-z_{n-1})} + A_4^{(n)} \mathrm{e}^{k\beta_n(z-z_n)})\mathrm{e}^{i(kx-\omega t)} \end{cases} \tag{3}$$

These equations indicate propagating harmonic waves in x-axis and standing waves in z-axis. $A_i^{(n)}$ is undetermined coefficient. $k = \omega/c$ is wave number. ω is the angular frequency. c is the phase velocity of a certain wave mode. α_n and β_n are defined as follow:

$$\alpha_n^2 = k^2\left(1 - \frac{c^2}{(c_L^{(n)})^2}\right), \ \beta_n^2 = k^2\left(1 - \frac{c^2}{(c_T^{(n)})^2}\right),$$

where $c_L^{(n)} = \sqrt{(\lambda_n + 2\mu_n)/\rho}$ and $c_T^{(n)} = \sqrt{\mu_n/\rho_n}$ represent the longitudinal and transverse wave velocities in each layer, respectively.

The boundary conditions encompass free surfaces at the top and bottom, as articulated in equation (4), and perfect bonding at each interface, as denoted in equation (5):

$$\begin{cases} \tau_{xz}^{(n)}(z) = 0 \\ \tau_{zz}^{(n)}(z) = 0 \end{cases} (n = 1, \ z = 0; \ n = N, \ z = z_N) \tag{4}$$

$$\begin{cases} u_x^{(n)}(z) = u_x^{(n+1)}(z) \\ u_z^{(n)}(z) = u_z^{(n+1)}(z) \\ \tau_{xz}^{(n)}(z) = \tau_{xz}^{(n+1)}(z) \\ \tau_{zz}^{(n)}(z) = \tau_{zz}^{(n+1)}(z) \end{cases} \tag{5}$$

in which

$$\begin{cases} n = 1, \quad z = z_1; \\ n = 2, \quad z = z_2; \\ \ldots; \\ n = N-1, \quad z = z_{N-1} \end{cases}$$

with $n = 1, \ z = z_1; \ n = 2, \ z = z_2; \ldots; \ n = N-1, \ z = z_{N-1}$. This yields $4 \times N$ undetermined coefficients subject to $4 \times N$ boundary conditions. Combining equations (2), (3), (4), and (5), the characteristic equation (6) is derived:

$$A\left[A_1^{(1)} A_2^{(1)} A_3^{(1)} A_4^{(1)} \cdots A_1^{(N)} A_2^{(N)} A_3^{(N)} A_4^{(N)}\right]^{\mathrm{T}} = 0 \tag{6}$$

where $\mathbf{A}$ represents the coefficient matrix of the undetermined coefficients. To ensure nontrivial solutions for equation (6), the determinant of the coefficient matrix $\mathbf{A}$ must be set equal to zero. Solving $|\mathbf{A}| = 0$ provides the dispersion curves for the specific layered structure. Subsequently, the coefficients in $\mathbf{A}$ are substituted into equation (2) to calculate the wave structures. Substituting a specific frequency and wave speed from the dispersion curve into equation (2) yields the wave structure of the corresponding guided wave mode at that frequency.

2.2 Guided waves in a bilayer plate

Figure 2 presents the outcomes of the computational analysis applied to a bilayer Al-Steel plate utilized in velocity verification and imaging experiments. This material combination, integrating the strength and cost-effectiveness of steel with the durability of aluminum, finds widespread applications ([26]). In Figure 2(a), relevant material parameters and thickness are depicted. For the assessment of interfacial defects, particular emphasis is placed on the application of interface wave modes, represented by the red curve in Figure 2.

Based on the wave structure characteristics of a specific guided wave mode, particularly the displacement concentration region of this mode, we can identify the first three orders of guided waves in the aluminum-steel plate as surface and interface wave modes, respectively. Analyzing the dispersion curves in Figure 2(b), it is observed that when the excitation frequency exceeds 0.5 MHz, the phase velocity of interface and surface wave modes tends to stabilize, indicating non-dispersiveness at high frequencies. Opting for 1 MHz as the excitation frequency and substituting the corresponding interface wave velocities (3029.8 m/s) into equation (2), the wave structures of the interface wave modes are computed, as illustrated in Figure 2(d). The vertical axis signifies the thickness of the layered plate, while the horizontal axis represents the normalized amplitude of displacement. Additionally, the wave structures of the two surface wave modes are calculated, corresponding to 2781.4 m/s for aluminum and 2846.4 m/s for steel.

Firstly, the dispersion curves reveal that both the interface and surface wave modes exhibit non-dispersive behavior in the high-frequency range. This non-dispersive characteristic holds significant advantages for defect

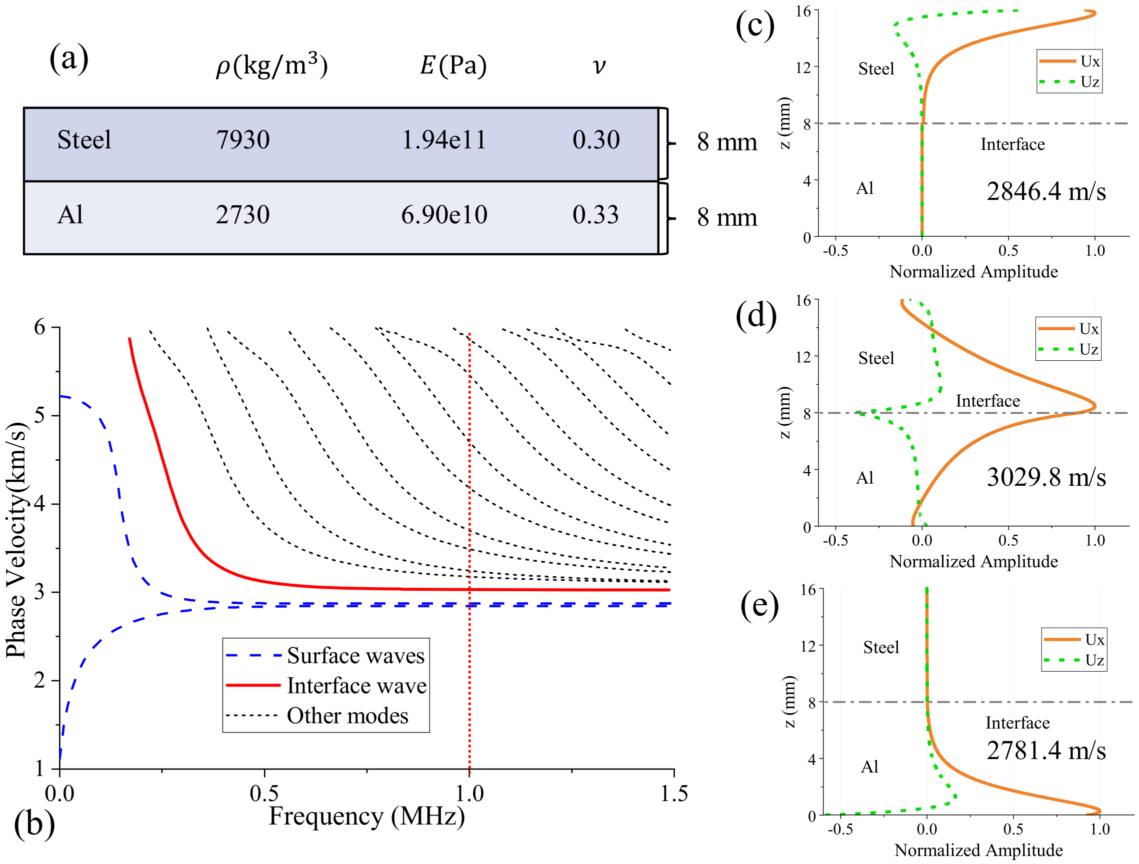

Figure 2. (a) Parameters for global matrix method. (b) Dispersion curves of a bilayer Al-Steel plate. (c–e) Wave structures of interface and surface wave modes.

localization in engineering applications, enhancing signal-to-noise ratio (SNR) and ensuring signal processing method robustness.

Secondly, the displacement of interface wave modes, or the energy associated with these modes, predominantly concentrates at the layered structure interfaces. This characteristic, while resembling conventional surface wave modes, distinguishes itself by being sensitive to internal interfaces. In contrast, surface wave modes typically detect defect on the structure's surface, observable through visual inspection or other non-destructive testing methods. The unique features of interface wave modes suggest the potential for extracting more comprehensive information about structural interfaces, laying a solid foundation for signal processing methods to achieve heightened defect recognition accuracy. Moreover, the energy peak tends towards the steel layer, suggesting that excitation on the steel layer may yield superior signal strength.

2.3 Experimental verification of interface and surface waves

Utilizing interface waves for interfacial defect imaging entails solving two a priori problems: 1. how to practically excite the interface wave modes; 2. experimental verification of the interface wave velocity.

Common methods for exciting interface waves include surface wave transducer technology and laser ultrasonic excitation technology ([27]), with surface wave transducer technology being particularly effective and convenient, as depicted in Figure 3.

The method initiates by generating surface waves on the composite plate's surface through a surface wave transducer. Surface waves are excited using the oblique incidence technique, which relies on Snell's law (Fig. 3(a)). The surface wave transducer ensures that the guided wave modes generated are predominantly surface wave modes with a wave velocity of approximately 2800 m/s [1]. This study applied "Doppler A*x*MHx-P14×14-SW surface wave transducers", as shown in Figure 3(d). "*x*MHz" indicates the center frequency of the transducer. Guided by the nature of guided waves, when the surface wave reaches the interface of the two material media, reflection, scattering, and transmission occur. The concept of wave structure matchability indicates that during wave mode conversion, the amplitude of guided wave modes in the transmitted wave, which are similar to the wave structure of the incident wave, is larger [28–30]. Figure 2(c–e) illustrates the similarity in wave structures between surface wave modes and interface wave modes, suggesting that interface waves remain dominant in the converted guided wave modes. The transmitted interface wave propagates forward along

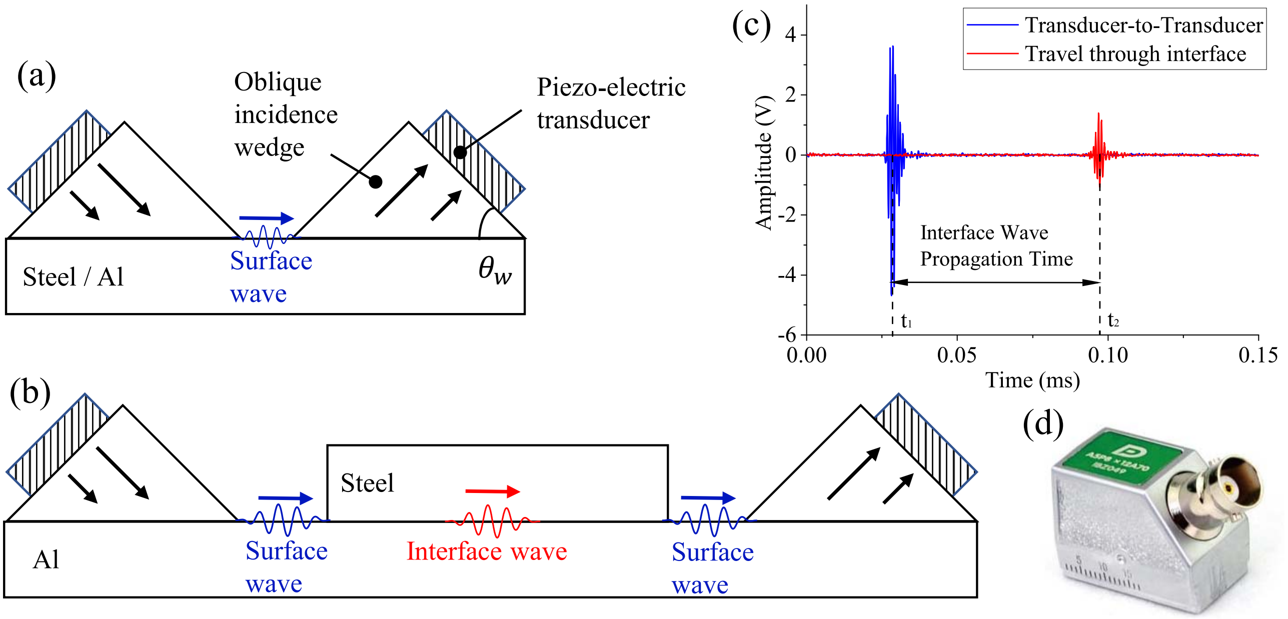

Figure 3. Principles of generating interface waves and interface wave velocity measurements. (a) Transducer-to-transducer propagation time measurement. (b) Interface wave propagation time measurement. (c) Raw signals in interface wave velocity verification experiments. (d) A surface wave transducer.

the interface and converts back into surface wave on the other side.

In the velocity verification experiment, initially, the two transducers are positioned opposite to each other, as in Figure 3(a), and the propagation time of the guided wave directly from one transducer to the other is measured as t_1. Subsequently, the two transducers are placed at the two ends of the interface, as in Figure 3(b), and the total propagation time of the guided wave is measured as t_2. The difference between t_1 and t_2 represents the propagation time of the interface wave, as in Figure 3(c). The waveforms in Figure 3(c) demonstrates high SNR and a single wave peak in the received wave packet. This indicates the propagation of a single guided wave mode in the experiment.

On this basis, this study systematically measured the group velocity values of aluminum-steel interface waves and the respective surface waves at different frequencies in the near-non-dispersive region. Among them, the measurement process of surface wave velocity is essentially identical to that of interface waves. The distinction lies in conducting the surface wave velocity measurement on a single-layer aluminum or steel plate (replacing the double-layer plate in Fig. 3(b) with a single-layer plate). The results are shown in Figure 4.

The reason for measuring the wave speed in the dispersion range is to verify that the absolute value of the wave speed and the trend of the wave speed change in the experiment are simultaneously the same as those predicted by the theory, and in this way to be sure that the guided wave modes generated in the experiment are indeed the guided wave modes depicted in the theoretical calculations. Therefore, mirrored aluminum and mirrored steel plates with a thickness of 3 mm, instead of 8 mm, were employed in the wave velocity validation experiments, resulting in different frequency coordinates in Figure 4 compared to Figure 2(b). Meanwhile, a surface wave transducer with a center frequency of 2.5 MHz was selected. In subsequent imaging experiments, non-dispersive interface waves will be selected for utilization.

It is essential to note that only the group velocity, representing the energy propagation velocity of guided wave modes, can be measured in the experiment. This differs from the phase velocity in Figure 2(b). The group velocity dispersion curve in Figure 4(a) is obtained by converting the group velocity c_g to the phase velocity c through the formula:

$$c_g = \frac{\mathrm{d}\omega}{\mathrm{d}k} = c^2\left(c - f\frac{\mathrm{d}c}{\mathrm{d}f}\right)^{-1} \quad (7)$$

Figure 4(b) zooms in on the experimentally measured aluminum-steel interface wave velocities compared to theoretical predictions. The red curve represents the theoretical group velocity profile of the interface wave, while the green triangles represent the experimental wave velocity measured at each frequency. The experimental wave velocity trend aligns with the red theoretical curve, albeit with the overall wave velocity absolute value slightly lower than the theoretical prediction. This systematic error is attributed to the epoxy bonding creating a thin layer at the interface with different material properties from the metal plate, making the experimental subject not exactly identical to the theoretical model. In practice, the tighter the bonding of the metal composite plate, the closer the experimental interface wave speed aligns with the theoretical wave speed, albeit

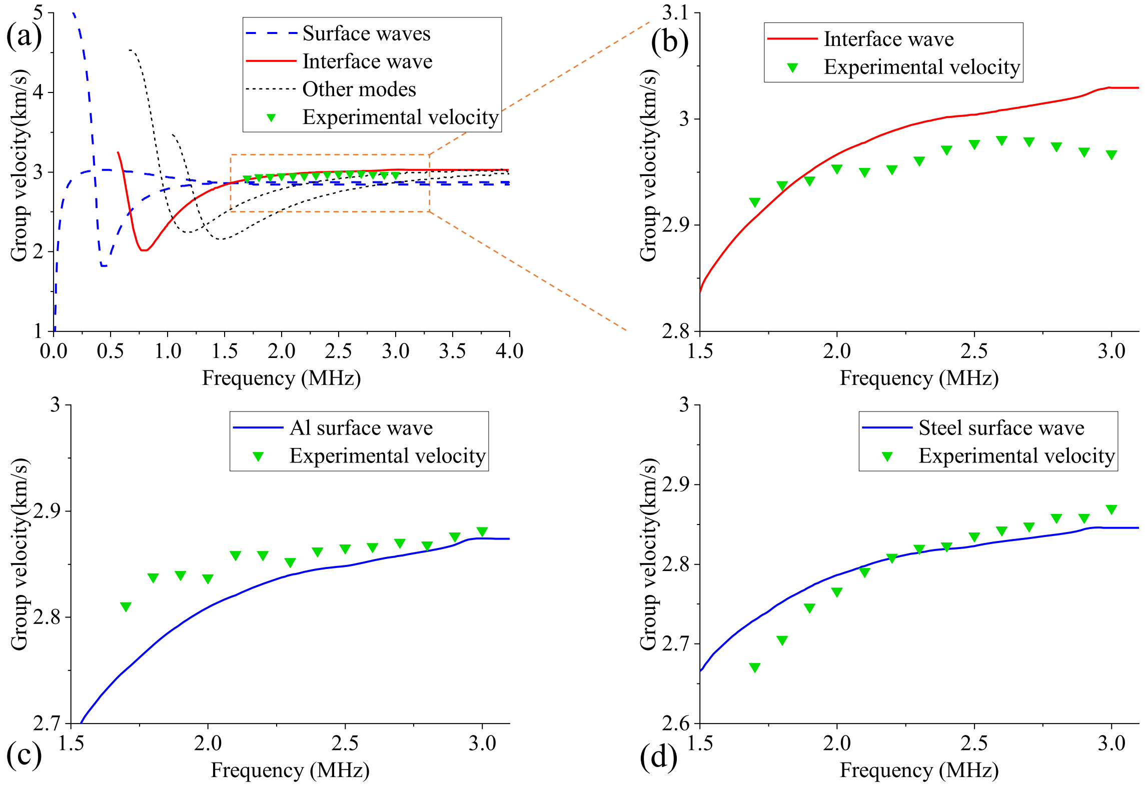

Figure 4. Experimental validation of the group velocities of (a) and (b) interface wave and (c) and (d) surface waves.

Table 1. Experimental Error Statistics for Wave Velocity Measurements.

Mode	Frequency at maximum error(MHz)	Theoretical velocity (m/s)	Experimental velocity (m/s)	Error
Al surface wave	1.8	2781.4	2853.4	2.5%
Steel surface wave	3.0	2846.4	2890.3	1.5%
Interface wave	2.9	3029.8	2949.7	2.6%

consistently slightly lower. In imaging work, positioning needs to be calibrated with the experimentally measured wave speed to enhance imaging accuracy. Figure 4(c, d) presents the experimental results of the surface wave velocity for aluminum and steel single-layer plates. These results strongly demonstrate that the detection system used in the study can excite pure surface and interface wave modes (Table 1).

The aforementioned findings establish the groundwork for advancing interfacial defect imaging through the utilization of interface waves. The errors identified in the results do not exert a substantial impact on imaging accuracy. This is attributed to further calibration of the interface wave speed in experiments, distinct from direct reliance on theoretical calculations. The comparative analysis of theoretical and experimental wave speeds serves to confirm the presence, detection maneuverability, and purity of interface wave modes within the experimental framework. This systematic approach, combining theoretical predictions and experimental validations, ensures a robust understanding of guided wave behavior in the studied bilayer Al-Steel plate. The successful generation and detection of interface wave modes pave the way for their application in interfacial defect imaging.

3 Elliptic tangent imaging algorithms

This section elaborates on the algorithms design aimed at imaging interfacial defect in a bilayer plate through the analysis of reflected interface wave signals.

3.1 Elliptic tangent reconstruction method

Drawing upon the performance characteristics of the surface wave transducer, this paper proposes an imaging method tailored for interfacial defect detection in a bilayer plate using reflected interface wave signals. Distinguished from traditional methods, the proposed elliptic tangent reconstruction method uniquely requires only two detection points to ascertain the location and orientation of the defect.

The principle of the elliptic tangent method, as applied in the experiment for synthesizing defect images, is illustrated in Figure 5. The surface wave transducer initiates surface waves that transform into interface waves upon

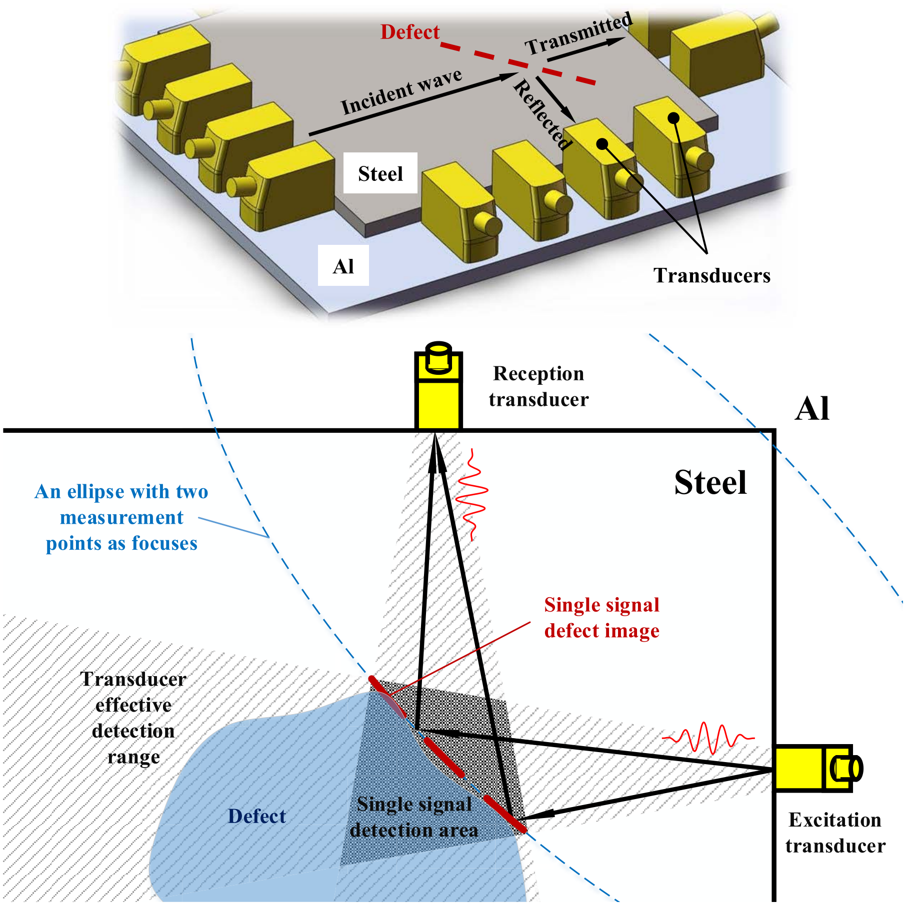

Figure 5. Principle of the elliptic tangent reconstruction method.

reaching the metal plates' interface. When encountering delamination defect, reflection and scattering occur, with a portion of the interface wave reflected back towards the reception transducer. This reflected signal, converted into surface waves, carries information about the defect. The time at which this wave peak occurs, adjusted by the interface wave velocity, provides the total distance of the defect from the two surface wave transducers:

$$d = c_g \cdot t$$

This distance d, regarded as the sum of elliptical focal radii, is used to plot an ellipse, as depicted by the dashed line in Figure 5.

The surface wave transducers in the test system exhibit limited excitation or reception capabilities within a relatively narrow effective detection range, as indicated by the diagonal shading in Figure 5. Consequently, the elliptical arc shown by the red bold dashed line is truncated based on the transducers' positions, confining the dashed ellipse to the dark shaded area. This section of the elliptical arc not only denotes the defect location but also reveals its orientation: a fundamental concept of the elliptic tangent method. By employing an array of transducers and overlaying the elliptic tangents from numerous detection signals, the final defect image is generated.

The pixel value of each pixel point in the overlaid image is calculated using the following formula:

$$I(x,y) = \sum_{i=1}^{N} s_i(t_i(x,y)) \cdot Q_{e,i}(x,y) \cdot Q_{r,i}(x,y) \qquad (8)$$

Here, $I(x,y)$ represents the pixel value of each pixel point; x, y are the coordinates of the pixel points; s_i is the time-domain amplitude information of the ith detection signal; $t_i(x,y)$ is the time for the surface wave to be sent out from the excitation transducer to the reception transducer for the ith detection signal, passing through the pixel points with coordinates of x, y; $Q_{e,i}(x,y)$, $Q_{r,i}(x,y)$ are the transmission coefficients, which indicates the effective ranges of the 0excitation transducer and the reception transducer corresponding to the ith detection signal, respectively. The transmission coefficients are reflected in the data as the weights for each pixel point, $0 < Q_i(x,y) < 1$. $Q_i(x,y) = 1$ when the pixel point is on the centerline of the effective range. The more the pixel point deviates from the centerline of the effective range, the more $Q_i(x,y)$ tends to 0. The summation is performed over all signals, and the transmission coefficients are applied based on the position of the pixel point relative to the effective range centerline (Table 1).

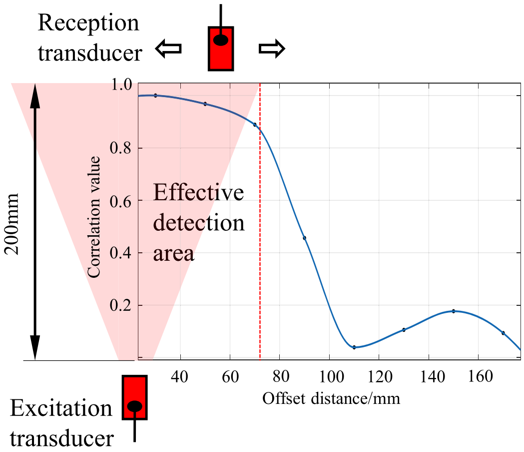

Figure 6. Experimental determination of the transducer transmission coefficient by correlation analysis.

The calculation of $t_i(x,y)$ is determined by the equation:

$$t_i(x,y) = \frac{\sqrt{(x-x_{e,i})^2 + (y-y_{e,i})^2} + \sqrt{(x-x_{r,i})^2 + (y-y_{r,i})^2}}{c} \tag{9}$$

where $x_{e,i}$, $y_{e,i}$ and $x_{r,i}$, $y_{r,i}$ represent the coordinates of the excitation and reception transducers for the ith detection signal, respectively, and c is the interface wave velocity.

The calibration of the transmission coefficient is identified as a fundamental a priori condition for the algorithm. In this investigation, the transmission coefficient of the oblique incidence surface wave transducer is determined through mutual correlation analysis, as depicted in Figure 6.

In the experimental setup, the excitation transducer is fixed, while the reception transducers, positioned 200 mm apart, are systematically shifted left and right to capture direct wave signals at various offset positions. These signals are then analyzed in correlation with the direct wave signals obtained at the 0 offset position to ascertain the transmission coefficient of the transducer. Mathematically, the cross-correlation between two signals is defined as:

$$CC = \max\left(\int_{-\infty}^{+\infty} s_{direct}(t) s_{offset}(t+\tau)\,\mathrm{d}t\right) \tag{10}$$

Here, τ denotes the time offset between the two signals, and CC represents the maximum correlation value attained between the signals $s_{direct}(t)$ and $s_{offset}(t)$. A higher CC value indicates a greater similarity between the signals [31].

The blue curve in Figure 6 serves as the fitting curve for the cross-correlation values between the direct path signal and other signals. The abscissa in the figure corresponds to the offset of the reception point in the vertical direction. It is notable that the cross-correlation values for offsets less than 70 mm exceed 0.8, with relatively minor differences among them. Conversely, when the offset exceeds 70 mm, the cross-correlation value experiences a rapid decline. Considering the dimensions of the experimental subject, the effective angle of the effective range of surface wave transducers is estimated to be approximately ±11°.

3.2 Pulse compression method

In subsequent imaging experiments, it was observed that directly utilizing the unprocessed reflected wave signals $s_i(t)$ for elliptic tangent defect reconstruction does not accurately capture the interfacial defect shape through simple superimposition of signal amplitudes. Two primary reasons contribute to this discrepancy:

1. In the experiment, to concentrate the frequency domain of the trigger signal, a multi-period sinusoidal modulation signal is employed to excite the guided wave. However, this choice results in a wide time-domain signal for the pulse signal. In the imaging outcomes, this wideness manifests as a broad boundary of the defect image, hindering the precise determination of defect contour.
2. The actual direction and extent of defect vary, leading to different scattering amplitudes for the interface wave. Consequently, certain defect boundaries in the imaging results appear excessively bright after superposition, while others appear relatively dark. This inconsistency complicates the judgment of defect morphology.

In summary, the compression of the time-domain signal of the guided wave is necessary to obtain a clear and distinct moment of the defect echo. Achieving the most accurate echo moments requires comprehensive information about the number of cycles, phase, residuals, and other parameters for each reflected wave packet during signal processing. Pulse compression serves as a deconvolution technique applied to enhance the resolution of received signals across various applications [32]. In time-domain signals, as encountered in ultrasonic testing, the presence of multiple wave packets is common. These signals can be expressed as the convolution of an incident signal $h(t)$ and a pulse sequence $x(t)$, accompanied by the inclusion of noise $n(t)$. This relationship is captured by the equation:

$$s(t) = x(t) * h(t) + n(t) \tag{11}$$

With direct measurements of $s(t)$ and $n(t)$, the pulse compression method facilitates the recovery of $x(t)$. However, certain crucial details, including the matching residual of the packets with the reference signals and their phase information, are inevitably lost during this process.

To address these challenges, orthogonal matching pursuit is employed as a method to process the raw signal. The orthogonal matching pursuit algorithm is one of the methods employed to derive sparse representations of signals [33]. This algorithm involves constructing an overcomplete atom dictionary and matching the atoms in the dictionary with the received signals. The weights of the matched signals are then calculated using the least squares method, enabling the capturing of multi-dimensional information related to the wave packets. In this method, for each peak at position p in $x(t)$, the corresponding atom is designed as:

$$g_\gamma(t) = 0.5 \times \left(1 - \cos\left(\frac{2\pi F(t-t_s)}{n}\right)\right)\sin(2\pi F(t-t_s)+\varphi) \tag{12}$$

Here, $\gamma = (F, n, t_s, \varphi)$. F represents the center frequency of the wave packet, n denotes the number of cycles, t_s signifies the time shift parameter, and φ corresponds to the phase parameter. This atom form is derived from the experimental trigger signal used to excite the interface wave in the experiment. Because the interface wave is non-dispersive in the high-frequency range, its waveform distortion during propagation is minimal. Thus, the matching signal can be directly constructed in the form of the trigger signal. The discrete interval of equation (12) to construct the dictionary should be chosen based on the actual experimental sampling interval. The center frequency F of the wave packet aligns with the excitation frequency, while the number of cycles n is linked to the number of cycles in the trigger signal. It is important to note that while the interface wave is non- dispersive, meaning the number of periods n remains unchanged during propagation, the actual number of periods of the reflected wave packet received in the experiment is larger than the number of periods of the trigger signal. The selection of n should be optimized based on the actual experimental signal. The time shift parameter t_s should span the entire time domain to achieve an overcomplete dictionary. However, after the signal undergoes pulse compression, the parameter is limited to a range near the peak position p. The phase shift parameter φ of the signal assumes values within the range $[0, 2\pi]$.

The overcomplete dictionary constructed at the peak position p is denoted as G, which encompasses a set of $g(t)$. In the process of matching pursuit, the approximate signal and matching residual are initialized as $\mathbf{s}(0) = \mathbf{0}$ and $\mathbf{R}(0) = \mathbf{s} - \mathbf{s}(0) = \mathbf{s}$, respectively. In the m-th iteration, the orthogonal matching pursuit algorithm searches for the atom in the dictionary with the largest inner product with the residual from the previous iteration, as described by the equation:

$$g_m = arg_{g\in\mathbf{G}}max\left|\langle\mathbf{R}^{(m-1)}, g\rangle\right| \tag{13}$$

Subsequently, the approximate signal can be calculated using the least squares method:

$$\mathbf{s}^{(m)} = arg_z min\,||\mathbf{s} - \mathbf{G}^{(m)}\mathbf{z}^{(m)}|| \tag{14}$$

where $\mathbf{G}(m)$ represents the set of the first m atoms, and $\mathbf{z}(m)$ is a vector comprising the first m coefficients. By repeating the above iterations, the sparse representation of wave packets in the received signals can be obtained. Finally, signals can be reconstructed as depicted in Figure 7.

The red curve in Figure 7 represents the signal reconstructed using the orthogonal matching pursuit algorithm, while the blue pulses denotes the exact timing information $x(t)$ of the reflected echoes extracted during the matching process. In this study, the stopping criteria of the pulse compression method are as follows:

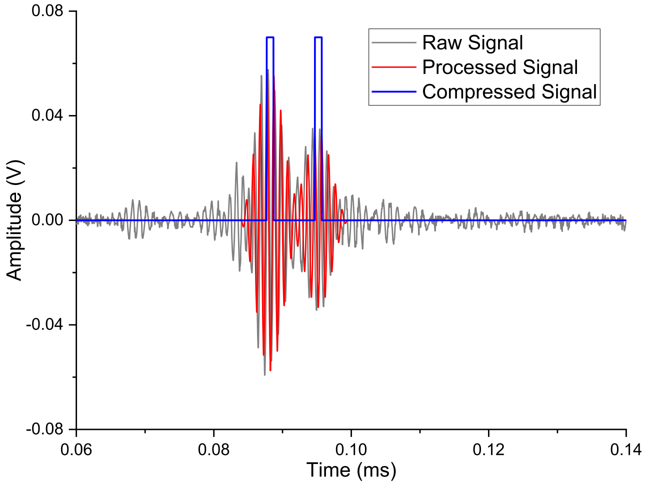

Figure 7. Comparison of the reflected waveform before and after the process of orthogonal matching pursuit.

1. The algorithm iterates until 3 atoms (waveforms) have been selected, which limits a reflected wave signal to contain at most 3 damage-reflected wave packets; or
2. The maximum amplitude of the matching residual $\mathbf{R}^{(m)}$ is less than 0.02 V, which is determined according to the SNR of the actual experimental signals to avoid too many interfering wave packets.

In the subsequent elliptic tangent defect reconstruction, $x(t)$ is utilized instead of the raw signal $s(t)$ mentioned in the previous subsection, as in equation (15):

$$I_c(x,y) = \sum_{i=1}^{N} x_i(t_i(x,y)) \cdot Q_{e,i}(x,y) \cdot Q_{r,i}(x,y) \tag{15}$$

The pixel values of the image using compressed signals $I_c(x,y)$ are then normalized according to equation (16):

$$I_c(x,y) = \begin{cases} 1 & \text{if } I_c(x,y) \geq 1 \\ 0 & \text{otherwise} \end{cases} \tag{16}$$

4 Interfacial defect imaging experiment

4.1 Experimental system and scheme

In this investigation, an automated detection system for surface wave transducer arrays was designed to achieve rapid transducer switching and the swift acquisition of a multitude of guided wave signals with diverse paths, enabling multiple repetitive measurements, as depicted in Figure 8.

The schematic of the hardware connections in the test system is illustrated in Figure 8(a), encompassing excitation and reception transducers 1 (Doppler A1MHz-P14×14-SW surface wave transducers), RF coaxial switch sets 2-1 and 2-2, Piezo EPA-104 signal amplifier 3, Tek 5032B arbitrary

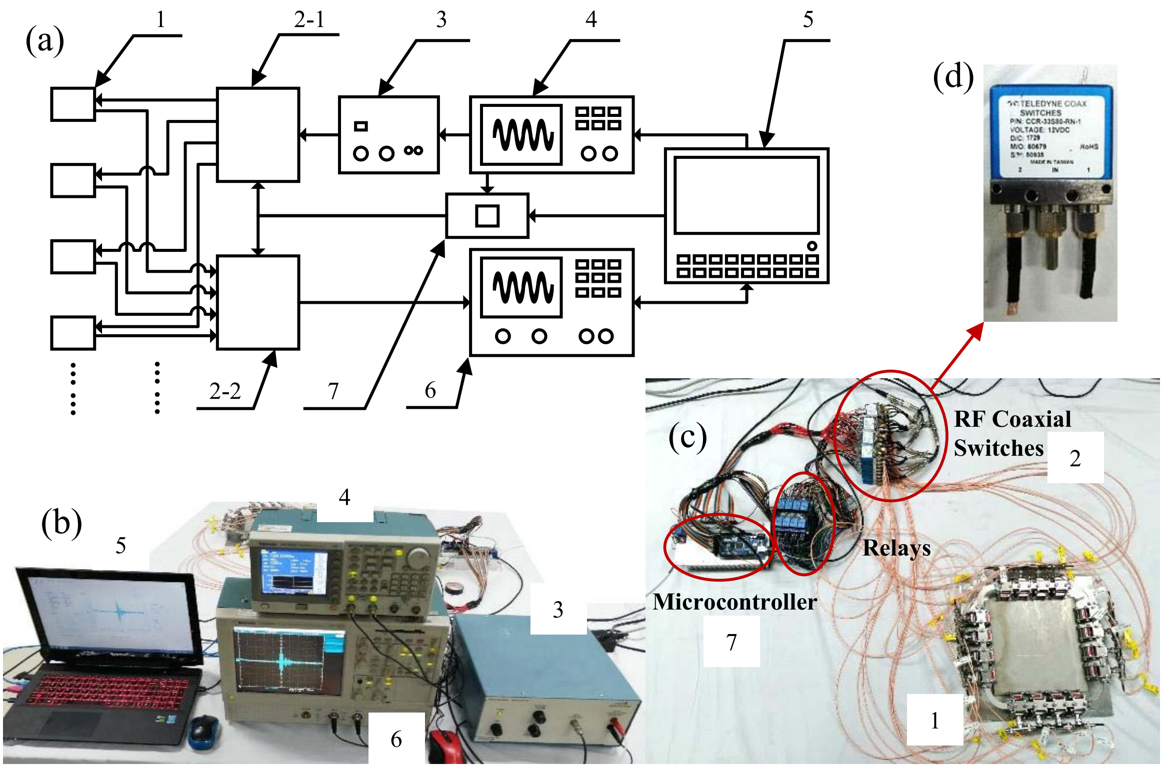

Figure 8. Automated detection system for interfacial defect imaging. (a) Schematic of the hardware connections. (b) Testing devices. (c) Transducers and relays arrangement. (d) An RF coaxial switch for high-frequency signals.

signal generator 4, PC 5, Tek TDS5032B oscilloscope 6, Arduino Mega 2560 microcontroller 7. The devices are shown in Figure 8(b). The system operates as follows: the PC 5 regulates the signal generator 4 to transmit a pulse signal, which is a 5-period sinusoidal wave modulated by the Hanning window. This signal's form aligns with the atoms of the dictionary used in the signal compression method. This signal is amplified by the signal amplifier 3, controlled by the RF coaxial switch group 2-1, transmitted to a surface wave transducer 1 for excitation, generating surface waves. RF coaxial switch group 2-2 controls a surface wave transducer 1 to receive the signal, transmitted to the oscilloscope 6 for temporary storage, and subsequently entered into the PC 5 for centralized preservation for subsequent imaging work. Simultaneously, the PC 5 generates TTL control signals to manage the on-off states of the two sets of relays through the microcontroller 7. The microcontroller 7 also receives the trigger signal from the signal generator 4 as a clock signal to control the relay switching frequency, achieving swift switching between transducers.

In the lower right corner of Figure 8(c) is the transducer array used in the experiment. The 16 transducers shown in the figure are collectively secured by the fixture designed and built for this study. This design allows for easy placement, removal, and replacement of all transducers simultaneously. The advantages of this design are demonstrated in this paper through multiple and rapid measurements.

For 1 MHz high-frequency electrical signals, ordinary electromagnetic relays introduce numerous interference components in the guided wave signals. To address this, RF coaxial switches were further controlled by ordinary relays. In this study, 32 single-pole, double-throw RF coaxial switches (Fig. 8(d)) were employed to manage 16 surface wave transducers, as illustrated in Figure 8(c, d). This configuration allows any transducer to function as either an excitation or reception transducer.

Figure 9 delineates the experimental subject testing scheme. In this illustration, 16 transducers sequentially serve as excitation transducers, while other 15 transducers sequentially fulfill the role of receivers. Consequently, each test generates a total of $15 \times 16 = 240$ signals. Due to the sparse transducer array used in this study and the substantial area of interfacial damage, the potential imaging enhancement from transmitted wave signals is minimal [34]. To enhance the algorithm's efficiency, this study does not consider the information from the transmitted wave packets in the imaging process; only the reflected wave packets are considered.

The experimental subject used in this study comprised a bilayer metal plate composed of a large and a small metal plate bonded together. Figure 9(b) displays the material before bonding. The larger plate measures 300 × 300 mm and is a 6061 aluminum alloy. The smaller plate, sized 200 × 200 mm, is a 304 stainless steel plate. A milled defect depth of 0.5 mm was precision-engineered on the surface of

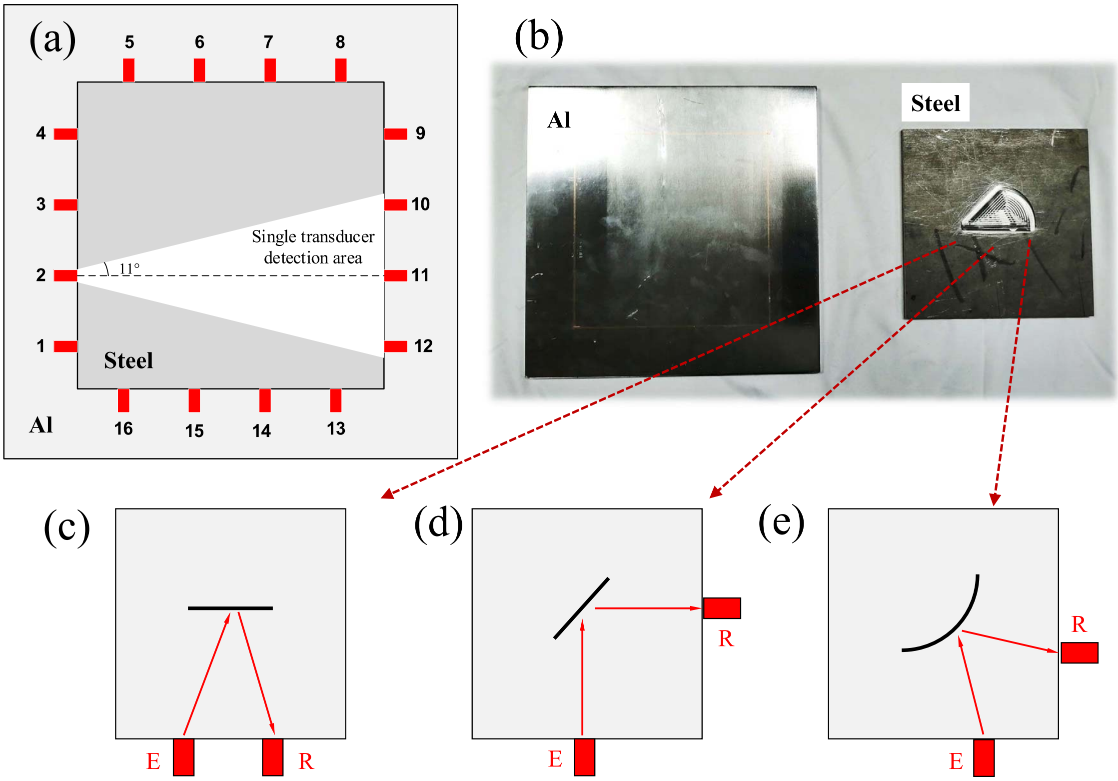

Figure 9. The tested Al-steel bilayer plate. (a) Configuration of transducers. (b) The two metal plates before bonding, featuring a pre-fabricated defect. (c–e) Principles illustrating various defect orientations.

the smaller steel plate to simulate interfacial delamination defect for imaging purposes. This artificially created defect includes vertical, oblique, and circular arc patterns, encompassing various defect morphologies encountered in industrial settings and effectively validating the imaging method's reliability (as depicted in Fig. 9(c)). Following the processing, the two metal plates were bonded using epoxy resin, and pressure was applied during solidification to maintain a continuous stress-strain boundary condition at the interface layer in line with the theoretical model.

Furthermore, a test subject of identical size and material, but without any induced defect, was created for comparative purposes in this study. The imaging results of the undamaged subject were compared to those of the damaged subject to assess the sensitivity of the proposed method in this paper.

4.2 Experimental results

The outcomes of the imaging experiments conducted on specimens both with and without defect are illustrated in Figure 10.

The results from multiple experiments employing this method are depicted in Figure 10. In the figure, the red dashed line delineates the actual interfacial defect contour, while the white dashed line represents the arrangement of the surface wave transducer, serving as a reference for image observation and method performance analysis. These experiments involved a 90° rotation of the specimen to assess the robustness of the imaging method. Specifically, in the experiment, variations in the coupling quality may impact the results of multiple tests. Additionally, rotating the measurement after 90° alters the spatial relationship between the test system and the tested object. This scenario is analogous to using the system to detect different damage.

A comparison of the imaging effects in the left column of the figure reveals the method's effectiveness in detecting delamination defect in the bilayer metal plate. The damaged experimental objects exhibit a distinct and clearly defined damaged area compared to the undamaged experimental objects, and there is no occurrence of detection leakage. Additionally, no artifacts are generated in the undamaged group. This substantiates the sensitivity of the imaging method to interfacial defect. However, utilizing the raw signal amplitude information for direct superimposition results in a fuzzy and cluttered depiction of the defect boundary, hindering the judgment of defect morphology.

Conversely, after compressing and processing the raw signal using the orthogonal matching pursuit algorithm, the defect reconstruction was re-executed, yielding the imaging results presented in the right column of the figure. In these results, the contrast between the presence and absence of defect remains apparent. Importantly, there is no occurrence of certain defect boundaries being markedly brighter than others, and all curves effectively represent the actual defect contour after combination. Furthermore, the positions of the curves in the image align well with

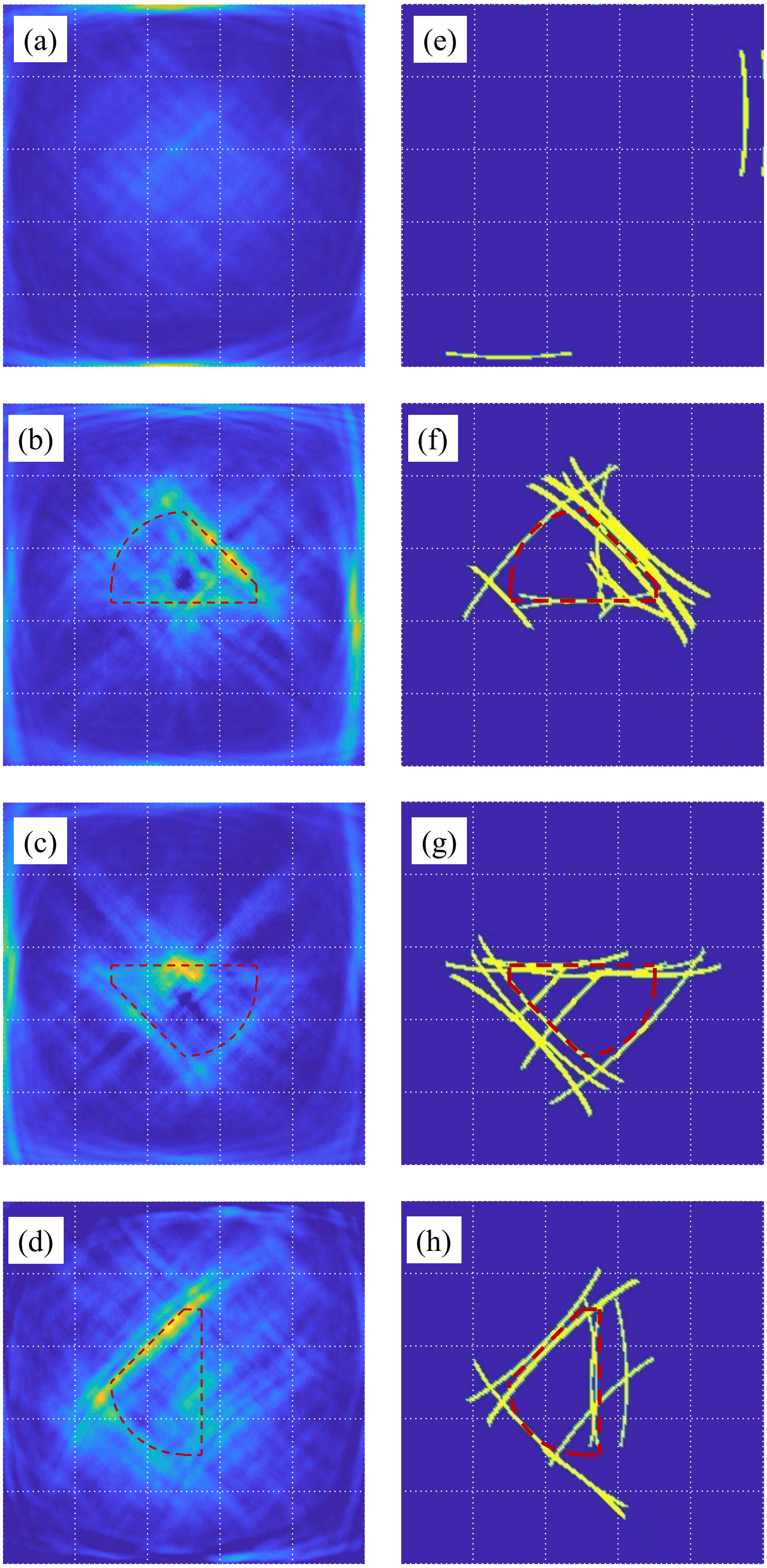

Figure 10. The imaging results of the interfacial defect. (a) and (e) Imaging results of undamaged test subjects. (a–d) Imaging results using the Hilbert transform of the raw signals. (e–h) Imaging results using the signals processed by orthogonal matching pursuit.

the actual defect boundaries, indicating high localization accuracy.

A detailed examination of each curve segment in the defect image reveals that the imaging method in the paper is most effective for oblique cracks (Fig. 9(d)), followed by straight cracks (Fig. 9(c)). Circular arc cracks (Fig. 9(e)) exhibit the poorest imaging effect, a characteristic determined by the transmission coefficient of the surface wave transducer. Under the transducer arrangement scheme outlined in the paper, when the excitation and reception transducers face different directions (Fig. 9(d)), their effective detection ranges have the largest overlap area, close to the midline of the effective range. Conversely, when the excitation and reception transducers are oriented in the same direction (Fig. 9(c)), the overlap of the effective detection range is limited. Additionally, the arc curve scatters the guided wave incident wave in all directions, diminishing the amplitude of the received guided wave for each individual transducer, resulting in the worst imaging effect. It is noteworthy that this paper's method easily allows for the addition of more transducers to form a denser transducer array, enhancing imaging accuracy. Moreover, the method, based on an economical guided-wave oblique incidence technique, enables rapid imaging of interfacial defect in layered metal plates with high accuracy, depicting the tangential direction of the defect. These advantages showcase the superiority of this imaging method over other NDT methods in terms of accuracy and cost.

5 Conclusions

Addressing the challenge of detecting interfacial defect in layered metal composite plates, this research introduces an elliptic tangent imaging method for interfacial defect assessment based on the interface wave modes of ultrasonic guided waves. The interface wave mode exhibits high-frequency non-dispersive characteristics, facilitating precise defect localization. Its energy concentration in the interface renders it particularly sensitive to interfacial defect. In experimental settings, the conversion of interface wave modes is achieved through the surface wave oblique incidence technique. The elliptic tangent imaging method leverages the transmission coefficient of the oblique incidence technique, enabling the simultaneous determination of defect location and orientation using only two transducers.

Experimental validation of wave velocity confirms that the guided wave mode generated corresponds to interface waves. The errors in surface and interface wave velocities do not exceed 2.6%, with the change trend aligning well with theoretical predictions. The study establishes an automatic detection system for interface waves, achieving the rapid switching of multiple transducers. Several repetitive experiments were conducted. In interfacial defect imaging experiments involving bilayer aluminum-steel plates, direct utilization of the Hilbert transform of the raw signal for defect reconstruction proves feasible but lacks precision. Conversely, employing the orthogonal matched pursuit algorithm for sparse representation of the raw signal results in a highly accurate detection of both the location and orientation of the defect.

Funding

This work is supported by the National Natural Science Foundation of China (Grant No.52275128).

Conflicts of interest

There are no relevant financial or non-financial competing interests to report.

Data availability statement

Data are available on request from the authors.

References

1. J.L. Rose: Ultrasonic guided waves in solid media, Cambridge University Press, London, 2014.
2. L.M. Brekhovskikh: Acoustics of layered media I: Plane and quasi-plane waves, Vol 5, Springer Science & Business Media, Berlin, German, 2012.
3. K.F. Graff: Wave motion in elastic solids, Courier Corporation, North Chelmsford, Massachusetts, USA, 2012.
4. H. Lamb: On waves in an elastic plate. Proceedings of the Royal Society of London. Series A, Containing Papers of a Mathematical and Physical Character 93, 648 (1917) 114–128.
5. L. Rayleigh: On waves propagated along the plane surface of an elastic solid. Proceedings of the London Mathematical Society 1, 1 (1885) 4–11.
6. R. Stoneley: Elastic waves at the surface of separation of two solids. Proceedings of the Royal Society of London. Series A, Containing Papers of a Mathematical and Physical Character 106, 738 (1924) 416–428.
7. A. Chattopadhyay, P. Kumari, V.K. Sharma: Reflection and refraction at the interface between distinct generally anisotropic half spaces for three-dimensional plane quasi-p waves. Journal of Vibration and Control 21, 3 (2015) 493–508.
8. J. Wang, Y. Zhang, Z. Zhang, C. Xue, B. Li: Directivity of quasi-sh0 modes in cubic anisotropic media. Ultrasonics 134 (2023), 107082.
9. M.D. Gardner, J.L. Rose, K.L. Koudela, C.A. Moose: Inspectability of interfaces between composite and metallic layers using ultrasonic interface waves. Proceedings of Meetings on Acoustics ICA2013 19, 1 (2013) 030105.
10. J.H. Bostron, J.L. Rose, C.A. Moose: Ultrasonic guided interface waves at a soft-stiff boundary. The Journal of the Acoustical Society of America 134, 6 (2013) 4351–4359.
11. P. Fromme, J.-P. Reymondin, B. Masserey: High frequency guided waves for disbond detection in multi-layered structures. Acta Acustica United with Acustica 103, 6 (2017) 932–940.
12. M. Mitra, S. Gopalakrishnan: Guided wave based structural health monitoring: A review. Smart Materials and Structures 25, 5 (2016) 053001.
13. A. Abid, D. Pereira, J.C. Fernandes, P. Belanger: Sensitivity study of ultrasonic guided waves to cortical bone mechanical properties with axial and circumferential propagation. Acta Acustica United with Acustica 103, 3 (2017) 421–429.
14. G. Zhao, B. Wang, T. Wang, W. Hao, Y. Luo: Detection and monitoring of delamination in composite laminates using

ultrasonic guided wave. Composite Structures 225 (2019) 111161.
15. B. Li, M.-H. Li, L. Tong: Interface waves in multilayered plates. The Journal of the Acoustical Society of America 143, 4 (2018) 2541–2553.
16. X. Zang, X. Zhao-Dong, L. Hongfang, C. Zhu, Z. Zhang: Ultrasonic guided wave techniques and applications in pipeline defect detection: A review. International Journal of Pressure Vessels and Piping 206 (2023) 105033.
17. R. Soman, K. Balasubramaniam, A. Golestani, M. Karpiński, P. Malinowski: A two-step guided waves based damage localization technique using optical fiber sensors. Sensors 20, 20 (2020) 5804.
18. D. Li, Z. Jing, M. Jin: Plate-like structure damage location identification based on lamb wave baseline-free probability imaging method. Advances in Mechanical Engineering 9, 1 (2017) 1687814016685702.
19. B. Feng, S. Cheng, K. Deng, Y. Kang: Localization of low-velocity impact in cfrp plate using time frequency features of guided wave and convolutional neural network. Wave Motion 119 (2023) 103127.
20. J. Moll, L. De Marchi, C. Kexel, A. Marzani: High resolution defect imaging in guided waves inspections by dispersion compensation and nonlinear data fusion. Acta Acustica United with Acustica 103, 6 (2017) 941–949.
21. J. Hua, X. Cao, Y. Yi, J. Lin: Time-frequency damage index of broadband lamb wave for corrosion inspection. Journal of Sound and Vibration 464 (2020) 114985.
22. Y. Liu, X. Hong, B. Zhang: A novel velocity anisotropy probability imaging method using ultrasonic guided waves for composite plates. Measurement 166 (2020) 108087.
23. G. Sha, M. Radzienski, R. Soman, T. Wandowski, M. Cao, W. Ostachowicz: Delamination imaging in laminated composite plates using 2d wavelet analysis of guided wave fields. Smart Materials and Structures 30, 1 (2020) 015001.
24. F. Honarvar, H. Sheikhzadeh, M. Moles, A.N. Sinclair: Improving the time-resolution and signal-to-noise ratio of ultrasonic nde signals. Ultrasonics 41, 9 (2004) 755–763.
25. M.M. Malatesta, D. Bogomolov, M. Messina, D. D'Ippolito, N. Testoni, L. De Marchi, A. Marzani: The delay multiply and sum algorithm for lamb waves based structural health monitoring, in European workshop on structural health monitoring: Special collection of 2020 papers-Volume 2, Springer, Berlin, German, 2021, pp. 657–666.
26. Hisao Kawase, Mamoru Makimoto, Kazuhiro Takagi, Youji Ishida, Takakazu Tanaka: Development of aluminum-clad steel sheet by roll-bonding. Transactions of the Iron and Steel Institute of Japan 23, 7 (1983) 628–632.
27. R.O. Claus, C.H. Palmer: Optical measurements of ultrasonic waves on interfaces between bonded solids. ITSU 27 (1980) 97–103.
28. D.A. Lee, D.M. Corbly: Use of interface waves for nondestructive inspection. IEEE Transactions on Sonics and Ultrasonics 24, 3 (1977) 206–211.
29. P. Puthillath, J.M. Galan, B. Ren, C.J. Lissenden, J.L. Rose: Ultrasonic guided wave propagation across waveguide transitions: Energy transfer and mode conversion. The Journal of the Acoustical Society of America 133, 5 (2013) 2624–2633.
30. Zhiyuan Zhang, Bing Li, Guangyuan Gao, Minghang Li: Measurement of wave structures of non-dispersive guided waves in opaque media. Measurement Science and Technology 32, 11 (2021) 115601.
31. Hu Yuting, Shuncai Li, Xing Deng, Slatin Vadim: Correlation analysis of noise sound pressure and vibration in aluminum alloy milling. Journal of Vibration and Control 28 (2020) 1077546320975977.
32. C.H. Wang, J.T. Rose, F.-K. Chang: A synthetic time-reversal imaging method for structural health monitoring: Smart Materials and Structures 13, 2 (2004) 415.
33. Stéphane G. Mallat, Zhifeng Zhang: Matching pursuits with time-frequency dictionaries. IEEE Transactions on Signal Processing 41, 12 (1993) 3397–3415.
34. Jiaqi Wang, Bing Li, Fanghao Pang, Yunfei Zhang: Imaging method of interfacial anomalies in layered structures. Journal of Vibration and Control 29 (2022) 10775463221089441.

Cite this article as: Wang J. Li B. & Zhang Y. 2024. Elliptic tangent imaging method for layered plate interfacial defects based on non-dispersive guided waves. Acta Acustica, **8**, 23.